

Highlights

Impacts of Hurricane Irma (2017) on wave-induced ocean transport processes

Thomas Dobbelaere, Milan Curcic, Matthieu Le Hénaff, Emmanuel Hanert

- The coupled SLIM+SWAN model correctly reproduced the hydrodynamics and waves during Irma.
- Wave radiation stress increased currents by up to 1 m/s during Irma.
- Wave radiation stress gradients were the largest on the shelf break and over reefs.
- Waves could deflect drifting particles by up to 20 km during the hurricane.
- The Stokes drift had an impact on transport 4 times larger than the wave radiation stress.

Impacts of Hurricane Irma (2017) on wave-induced ocean transport processes

Thomas Dobbelaere^{a,*}, Milan Curcic^b, Matthieu Le Hénaff^{c,d}, Emmanuel Hanert^{a,e}

^a*Eath and Life Institute (ELI), UCLouvain, Louvain-la-Neuve, Belgium*

^b*Rosenstiel School of Marine and Atmospheric Sciences (RSMAS), University of Miami, Coral Gables, Florida, USA*

^c*Cooperative Institute for Marine and Atmospheric Studies (CIMAS), University of Miami, Miami, Florida, USA*

^d*Atlantic Oceanographic and Meteorological Laboratory (AOML), NOAA, Miami, Florida, USA*

^e*Institute of Mechanics, Materials and Civil Engineering (IMMC), UCLouvain, Louvain-la-Neuve, Belgium*

Abstract

The [intensity](#) of major tropical cyclones has increased during the past decade. Their effect is particularly acute in coastal areas where they cause extensive damage leading to an influx of debris, sediments and waste to the sea. However, most operational coastal ocean models do not represent heavy-wind transport processes correctly [if](#) the hydrodynamics is not coupled with the wind-generated waves. This may lead to significant errors in ocean simulations under tropical cyclone conditions. Here, we investigate current-wave interactions during a major hurricane and assess their impact on transport processes. We do that by coupling the unstructured-mesh coastal ocean model SLIM with the spectral wave model SWAN, and applying it to the Florida Reef Tract during Hurricane Irma (September 2017). We show that the coupled model successfully reproduces the wave behavior, the storm surge and the ocean currents during the passage of the hurricane. We then use

*Corresponding author

Email address: thomas.dobbelaere@uclouvain.be (Thomas Dobbelaere)

the coupled and uncoupled wave-current model to simulate the transport of passive drifters. We show that the wave radiation stress gradient alone can lead to changes of up to 1 m/s in the modeled currents, which in turn leads to differences of up to 5 km in the position of drifting material over the duration of the hurricane. The Stokes drift however appears to cause deflections up to 4 times larger and hence dominates wave-induced transport. Wave-current interactions therefore strongly impact the transport of drifting material such as sediments and debris in the aftermath of a hurricane. They should thus be taken into account in order to correctly assess its overall impact.

Keywords: Hurricane, Ocean transport, Wave-current interactions, Stokes drift, Unstructured mesh ocean model

1 1. Introduction

2 Major hurricanes are becoming more [intense](#) under the effect of global
3 warming (Bhatia et al., 2019; Knutson et al., 2020). Better understanding their
4 repercussions on coastal areas becomes therefore critical. However, estimating
5 the impact of hurricanes on the coastal ocean circulation remains a challenge.
6 Understanding wave-current interactions and representing their impact on
7 coastal ocean transport processes is central to many coastal activities such
8 as dredging, erosion management, oil and gas activities, search and rescue,
9 and insurance (Bever and MacWilliams, 2013; Li and Johns, 1998; Breivik
10 et al., 2013). All these activities require wave-current models to predict the
11 impact of tropical cyclones on the coastal circulation and on the sea surface
12 elevation.

13 Wave-current interactions during a cyclone are highly nonlinear and vary
14 significantly in space and time (Wu et al., 2011). Wave-induced currents
15 are generated by wave radiation stress gradients (Longuet-Higgins, 1970),
16 affecting water levels near shorelines and wave breaking points (Longuet-
17 Higgins and Stewart, 1964). Changes in water levels and currents, in turn,
18 affect the motion and evolution of the waves (Sikirić et al., 2013). Coupled

19 wave-current models hence require the calculation of the full directional wave
20 spectrum in order to correctly reproduce the dynamics of wind-driven surface
21 waves. This is usually achieved by spectral wave models, which describe the
22 evolution of the wave energy spectrum. As of today, the most popular spectral
23 wave models are [the WAve Model](#) (WAM) (WAMDI Group, 1988), [Simulating](#)
24 [WAve Nearshore](#) (SWAN) (Booij et al., 1999), and WAVEWATCH III (Tolman
25 et al., 2009). Among these models, SWAN has been specifically developed for
26 coastal applications, as it represents depth-induced wave breaking and triad
27 wave-wave interactions using numerical techniques adapted to small-scale,
28 shallow water regions (Booij et al., 1999). WAVEWATCH III has also recently
29 been equipped with new parallelization algorithm, domain decomposition and
30 numerical schemes for high resolution coastal applications (WW3DG, 2019;
31 Abdolali et al., 2020).

32 Coastal oceans are characterized by the complex topography of the coast-
33 line and the presence of islands, reefs and artificial structures. Traditional
34 structured-grid models lack the flexibility to simulate near-shore processes at
35 a sufficiently small scale. Although the use of nested structured grids allows
36 local grid refinement (Warner et al., 2010), staircase-like representation of
37 complex coastal topographies cannot be avoided. Instead, unstructured-mesh
38 models easily adapt to the topography and are hence better suited to coastal
39 processes (Fringer et al., 2019). Capturing the impact of the topography on
40 wave interactions becomes even more important in the case of tropical cy-
41 clones. Heavy winds generate large wind-waves and disturb ocean conditions
42 (Liu et al., 2020) by causing coastal upwellings on continental shelves (Smith,
43 1982) and inducing strong currents, waves and storm surges in nearshore and
44 coastal regions (Dietrich et al., 2010; Weisberg and Zheng, 2006).

45 Ocean waves act as the dynamical interface between the atmosphere and
46 the ocean. Through this interface, tropical cyclones cause a cooling of the
47 upper ocean layer by vertical mixing and heat transfer (Aijaz et al., 2017;
48 Varlas et al., 2020). By altering the structure of the upper-ocean, hurricane

49 can cause the disruption of major ocean currents such as the Florida Current
50 and Gulf Stream (Oey et al., 2007). Interaction with hurricanes alters the
51 thermal structure of these currents and can cause a significant decline of their
52 flow, resulting in delayed increased coastal levels along their path, even in
53 locations out of reach of the hurricane itself (Ezer et al., 2017; Ezer, 2018,
54 2020).

55 Near the storm, heavy wind conditions also affect material transport at
56 the ocean surface. The transport of drifting objects or substances that are
57 locally released is often best represented by a Lagrangian individual-based
58 model. Such an approach is routinely used to model the dispersal of larvae,
59 pollutants, sediments and many other tracers (e.g. Le Hénaff et al., 2012;
60 Liubartseva et al., 2018; Figueiredo et al., 2013; Frys et al., 2020). Although
61 some transport model might take wave-induced currents into account, most
62 of them neglect wave-current interactions, which can lead to significant errors
63 in storm conditions (Röhrs et al., 2012; Curcic et al., 2016). Niu and Xia
64 (2017) and Mao and Xia (2018, 2020) investigated the impact of wave-current
65 interactions during storm event in lakes and inlets. However, to our knowledge,
66 there have been no similar studies on the impact of hurricane-induced wave-
67 current interactions in coastal environments such as the Florida Reef Tract
68 (FRT), where changes in transport processes might significantly impact the
69 biological connectivity.

70 The main questions we want to answer are the following: (1) How impor-
71 tant are wave-current interactions during a tropical cyclone? (2) What effect
72 do they have on the transport of drifting material? We tackle these issues by
73 investigating the transport of drifting particles on the Florida shelf during
74 Hurricane Irma, one of the strongest and costliest tropical cyclones on record
75 in the Atlantic Basin (Xian et al., 2018), which made landfall in Florida in
76 September 2017. To do that, we developed an unstructured-mesh coupled
77 wave-current model of the whole FRT to simulate the ocean circulation un-
78 der hurricane conditions. Both modeled currents and waves were validated

79 against field measurements and then used to simulate the transport of drifting
80 material in the Florida Keys and over the Florida inner shelf. Model outputs
81 were then compared with uncoupled simulation results in order to assess
82 the impact of the radiation stress gradient and Stokes drift on the modeled
83 currents and transport.

84 **2. Methods**

85 *2.1. Study area and observational data*

86 We study the ocean circulation in an area that covers the whole FRT
87 and includes the northwestern end of the Gulf of Mexico and the Straits of
88 Florida (Fig. 1). The large-scale ocean circulation around South Florida
89 is dominated by the Florida Current (FC), which originates from the Loop
90 Current (LC) where it enters the Florida Straits from the Gulf of Mexico, and,
91 downstream, forms the Gulf Stream. The FC is a major western boundary
92 current characterized by spatial variability and meandering, associated with
93 the presence of cyclonic eddies between the core of the current and the
94 complex reef topography of the FRT (Lee et al., 1995; Kourafalou and Kang,
95 2012). The variability of the FC extends over a large range of spatial and
96 temporal scales, with periods of 30-70 days in the Lower Keys (Lee et al., 1995)
97 and shorter periods of 2-21 days in the Upper Keys (Lee and Mayer, 1977),
98 and exhibits significant seasonal and interannual cycles (Johns and Schott,
99 1987; Lee and Williams, 1988; Schott et al., 1988). Circulation on the West
100 Florida Shelf (WFS), on the other hand, is forced by local winds and tidal
101 fluctuations (Lee and Smith, 2002; Liu and Weisberg, 2012). Furthermore,
102 due to its location relative to the warm waters of the North Atlantic, Florida
103 is particularly vulnerable to tropical cyclones. On average, the state is hit by
104 a hurricane every two years and strong hurricanes, some of which are among
105 the most destructive on record, strike Florida on average once every four
106 years (Malmstadt et al., 2009).

107 The state of the ocean around Florida is monitored by an extensive
108 array of tide gauges, current meters and buoys. In this study, we used sea
109 surface elevation measurements from the National Oceanic and Atmospheric
110 Administration's (NOAA) Tides and Currents dataset. These measurements
111 were taken at four locations: two in the Florida Keys (Key West and Vaca
112 Key); one on the East coast of Florida (Virginia Key); and one on the West
113 coast (Naples). For the currents, we used ADCP measurements from the
114 University of South Florida's College of Marine Science's (USF/CMS) Coastal
115 Ocean Monitoring and Prediction System (COMPS) for the WFS (Weisberg
116 et al., 2009). More specifically, we used measurements from moorings C10,
117 C12 and C13, respectively located at the 25, 50, and 50 m isobaths of the
118 WFS (Liu et al., 2020). Finally, for the waves, we used measurements from
119 four buoys of the NOAA's National Data Buoy Center (NDBC); two on
120 Florida's eastern shelf and two on the WFS. The locations of all measurement
121 stations are shown in Fig. 1.

122 *2.2. Wind and atmospheric pressure during Hurricane Irma*

123 Hurricane Irma made landfall in Florida on 10 September 2017 as a
124 category 4 hurricane at Cudjoe Key (Florida Keys) and later as a category
125 3 hurricane on Marco Island, south of Naples (see hurricane track in Fig.
126 1). It then weakened to a category 2 hurricane as it moved further inland
127 (Cangialosi et al., 2018). The storm damaged up to 75% of the buildings at its
128 landfall point in the Florida Keys, making it one of the strongest and costliest
129 hurricanes on record in the Atlantic basin (Xian et al., 2018; Zhang et al.,
130 2019). The strongest reported sustained winds on Marco Island were 50 m/s
131 while the highest recorded storm surge was 2.3 m, although larger wind speed
132 likely occurred in the Florida Keys (Pinelli et al., 2018). To reproduce the
133 wind profile of Irma in our model, we used high-resolution H*Wind wind fields
134 (Powell et al., 1998). As these data represent 1-min averaged wind speeds,
135 we multiplied them by a factor 0.93 to obtain 10-min averaged wind speeds
136 (Harper et al., 2010). **This operation reduces the erratic values caused by the**

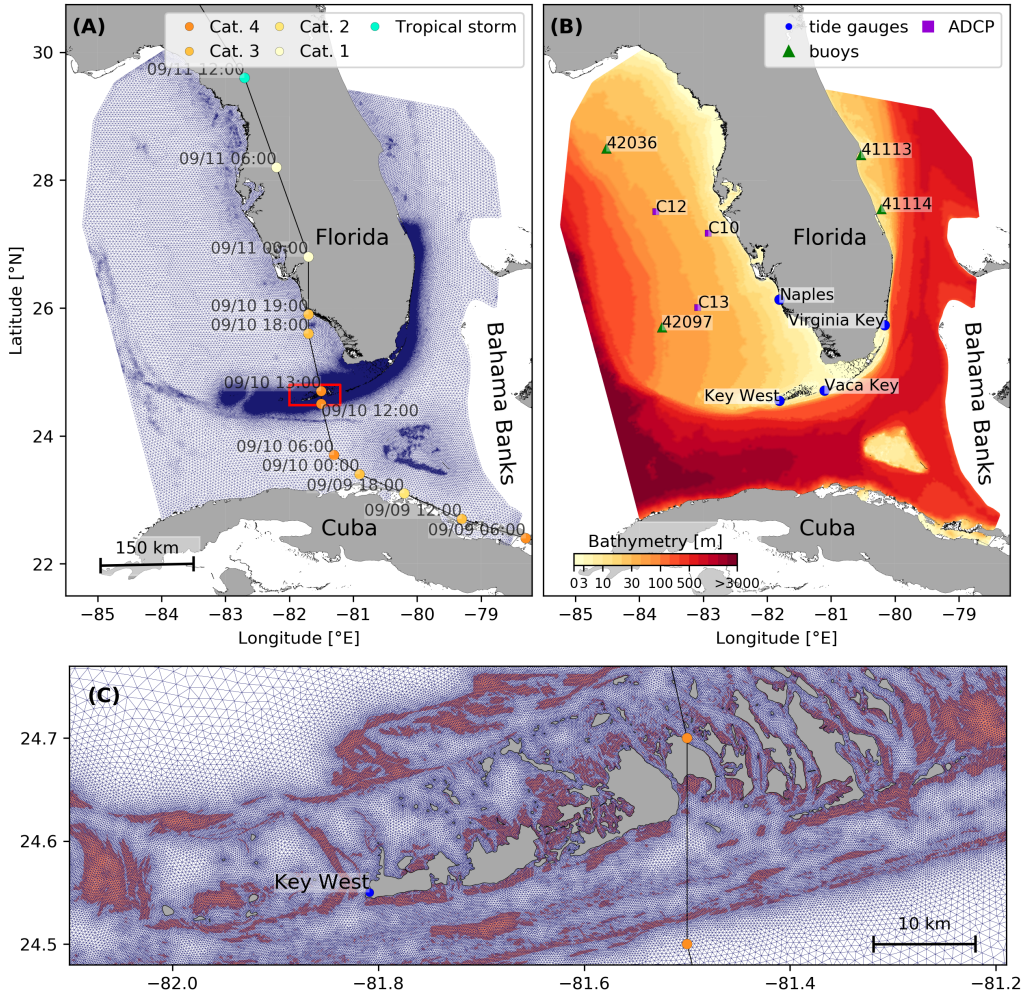


Fig. 1: (A) Mesh of the computational domain with the trajectory of Irma. The category of the hurricane is given by the Saffir-Simpson color scale. (B) Bathymetry of the domain with the location of stations used for the validation of the model outputs. (C) Close up view of the Lower Keys area (red box in (A)), where the mesh resolution reaches 100 m near reefs (shown in dark orange) and islands (shown in dark grey)

137 greater variance of mean winds measured over periods shorter than 10 minutes.
138 Furthermore, H*Wind wind profiles did not cover the whole model extent
139 during the passage of the hurricane and were thus blended within a coarser
140 wind field extracted from the European Centre for Medium-Range Weather
141 Forecasts (ECMWF) ERA-5 dataset (Fig. 2A). The pressure field during
142 the passage of Hurricane Irma was also reconstructed using ERA-5 data.
143 However, the coarse resolution of the dataset smoothes out the depression
144 at the center of the hurricane, leading to an underestimation of the pressure
145 gradient (Fig. 2B). To better capture the central depression of Irma, we
146 therefore built a hybrid pressure field using the position and the minimal
147 pressure of the core of the hurricane based on its track, as recorded in the
148 HURricane DATabases (HURDAT) 2 (Landsea and Franklin, 2013). Based on
149 this information, the hybrid pressure field was constructed by combining an
150 idealized Holland pressure profile (Lin and Chavas, 2012) within the radius of
151 maximum wind speed of Irma (Knaff et al., 2018) with ERA-5 pressure field.
152 The transition from the Holland profile to ERA-5 data outside the radius of
153 maximum wind speed data was performed using a smooth step function (Fig.
154 2).

155 *2.3. Hydrodynamic model*

156 Ocean currents generated during Hurricane Irma around South Florida
157 were modeled using the 2D barotropic version of the unstructured-mesh
158 Second-generation Louvain-la-Neuve Ice-ocean Model¹ (SLIM) (Lambrechts
159 et al., 2008). The model mesh covers an area similar to the model extent of
160 Dobbelaere et al. (2020), that includes the FRT but also the Florida Straits
161 and part of the Gulf of Mexico (Figure 1). However, this area has been slightly
162 extended northeastward and westward in order to include the NOAA-NDBC
163 buoys. Furthermore, to withstand potential cell drying during the hurricane,

¹<https://www.slim-ocean.be>

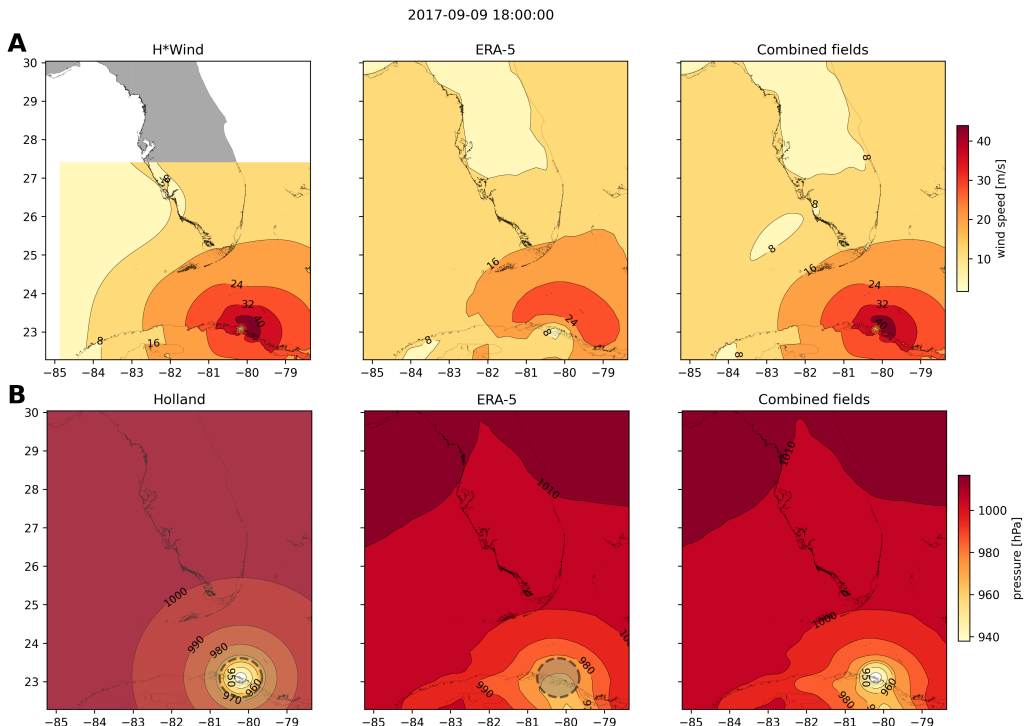


Fig. 2: Snapshot of the hybrid wind (**A**) and pressure (**B**) profiles constructed to capture the passage of Hurricane Irma at 1800 UTC on 9 September 2017. Wind profiles were obtained by combining high resolution H*Wind with coarser ERA-5 wind fields. The pressure field was built by combining the ERA-5 pressure field with an idealized Holland pressure profile based on the track of Irma in the HURDAT 2 database. Holland field was only used within the radius of maximum wind speed (dashed grey line) of the hurricane to capture its central depression.

164 we solved the conservative shallow water equations with wetting-drying:

$$\begin{aligned} \frac{\partial H}{\partial t} + \nabla \cdot (\mathbf{U}) &= 0, \\ \frac{\partial \mathbf{U}}{\partial t} + \nabla \cdot \left(\frac{\mathbf{U}\mathbf{U}}{H} \right) + f\mathbf{e}_z \times \mathbf{U} &= \alpha g H \nabla(H - h) - \frac{1}{\rho} \nabla p_{\text{atm}} + \frac{1}{\rho} \boldsymbol{\tau}_s \\ &\quad + \nabla \cdot (\nu \nabla \mathbf{U}) - \frac{C_b}{H^2} |\mathbf{U}| \mathbf{U} + \gamma (\mathbf{U}_{\text{ref}} - \mathbf{U}), \end{aligned} \quad (1)$$

165 where H is the water column height and \mathbf{U} is the depth-averaged transport;
166 f is the Coriolis coefficient; g is the gravitational acceleration; h is the
167 bathymetry; α is a coefficient indicating whether the mesh element is wet
168 ($\alpha = 1$) or dry ($\alpha = 0$) (Le et al., 2020); ν is the Smagorinsky viscosity; C_b is
169 the bulk bottom drag coefficient; p_{atm} is the atmospheric pressure; $\boldsymbol{\tau}_s$ is the
170 surface stress, usually due to wind; and γ is a relaxation coefficient towards
171 a reference transport \mathbf{U}_{ref} . As this study focuses on transport processes
172 and not coastal flooding, wetting-drying is only applied on wet grid cells
173 that may become dry under the influence of the hurricane. As in Frys et al.
174 (2020) and Dobbelaere et al. (2020), SLIM currents were gradually relaxed
175 towards the operational Navy HYbrid Coordinate Ocean Model (HYCOM)
176 product (GOMl0.04², Chassignet et al. (2007)) in regions where the water
177 depth exceeds 50 m. HYCOM's 3D currents were depth-integrated into 2D
178 transports to be used as forcing in the model. Moreover, these transports as
179 well as HYCOM's sea surface elevation were used as boundary condition in
180 the model.

181 We adapted the parameterization of the wind-induced surface stress to
182 storm conditions. At very high wind speeds, the white cap is blown off
183 the crest of the waves. This phenomenon, also known as spume, has been
184 hypothesized to generate a layer of droplets that acts as a slip layer for the

2<https://www.hycom.org/data/goml0pt04>

185 winds at the ocean-atmosphere interface (Holthuijsen et al., 2012). It causes
 186 a saturation of the wind drag coefficient for strong winds (Powell et al., 2003;
 187 Donelan et al., 2004; Curcic and Haus, 2020). We take this saturation effect
 188 into account by using the wind drag parameterization of Moon et al. (2007).
 189 In this parameterization, the drag coefficient C_d depends on the wind speed
 190 at 10-m height U_{10} according to:

$$C_d = \kappa^2 \log \left(\frac{10}{z_0} \right)^{-2} \quad (2)$$

191 where κ is the von Karman constant and z_0 is the roughness length expressed
 192 as:

$$z_0 = \begin{cases} \frac{0.0185}{g} u_*^2 & \text{if } U_{10} \leq 12.5 \text{ m/s ,} \\ [0.085(-0.56u_*^2 + 20.255u_*) & \text{if } U_{10} > 12.5 \text{ m/s ,} \\ +2.458] - 0.58] \times 10^{-3} \end{cases} \quad (3)$$

193 with u_* the friction velocity. The relation between U_{10} and u_* is given by:

$$U_{10} = -0.56u_*^2 + 20.255u_* + 2.458 . \quad (4)$$

194 The mesh resolution depends on the distance to the coastlines and reefs
 195 following the approach of Dobbelaere et al. (2020). The mesh is then further
 196 refined according to bathymetry value and gradient, as suggested in the
 197 SWAN user-guide³. Such an approach improves the model efficiency as the
 198 mesh resolution is only increased where required by the currents and waves
 199 dynamics. The mesh was generated with the seamsh⁴ Python library, which is
 200 based on the open-source mesh generator GMSH (Geuzaine and Remacle,
 201 2009). It is composed of approximately 7.7×10^5 elements. The coarsest
 202 elements, far away from the FRT, have a characteristic length of about 5 km

³<http://swanmodel.sourceforge.net/unswan/unswan.htm>

⁴<https://pypi.org/project/seamsh/>

203 whereas the finest elements have a characteristic length of about 100 m along
204 the coastlines and over the reefs (Fig 1).

205 *2.4. Wave model*

206 Waves were modeled using the parallel unstructured-mesh version of the
207 Simulating WAves Nearshore (SWAN) model (Booij et al., 1999), one of the
208 most popular wave models for coastal areas and inland waters. It solves the
209 action balance equation (Mei, 1989):

$$\frac{\partial N}{\partial t} + \nabla_{\mathbf{x}} \cdot [(\mathbf{c}_g + \mathbf{u})N] + \frac{\partial}{\partial \theta}[c_\theta N] + \frac{\partial}{\partial \sigma}[c_\sigma N] = \frac{S_{in} + S_{ds} + S_{nl}}{\sigma}, \quad (5)$$

210 where $N = E/\sigma$ is the wave action density and E is the wave energy spectrum;
211 θ is the wave propagation direction; σ is the intrinsic wave frequency; \mathbf{c}_g is
212 the wave group velocity, $\mathbf{u} = \mathbf{U}/H$ is SLIM depth-averaged current velocity;
213 c_θ and c_σ are the propagation velocities in spectral space due to refraction
214 and shifting in frequency due to variations in depth and currents; and S_{in} ,
215 S_{ds} , and S_{nl} respectively represent wave growth by wind, wave decay and
216 nonlinear transfers of wave energy through four and three-wave interactions,
217 *i.e.* quadruplets and triplets. The wave spectra were discretized with 48
218 direction bins and 50 frequency bins logarithmically distributed from 0.03 to
219 2 Hz. Exponential wind growth was parameterized using the formulation of
220 Janssen (1991), while dissipations by whitecapping and bottom dissipation
221 followed the formulations of Komen et al. (1984) and Madsen et al. (1989),
222 respectively.

223 Coefficients for exponential wind growth and whitecapping parameteriza-
224 tions were based on the results of Siadatmousavi et al. (2011), and significantly
225 differ from SWAN's default settings. By default, SWAN implements the wind
226 input formulation of Komen et al. (1984) and the steepness-dependent co-
227 efficient governing dissipation by whitecapping is a linear function of the
228 wavenumber. In this study, this steepness-dependent coefficient is a quadratic
229 function of the wavenumber, as it showed better predictions of the significant

230 wave height in the study of Siadatmousavi et al. (2011). The choice of these
 231 formulations was motivated by the appearance of numerical instabilities in
 232 the region of the Gulf Stream when using SWAN's default parameter values.
 233 Finally, ERA-5 wave spectra was used as boundary condition for SWAN.
 234 Wave spectra is obtained from the ocean wave model WAM and is given on a
 235 $1^\circ \times 1^\circ$ grid with 24 directions and 36 frequencies.

236 Surface waves induce a net drift in the direction of the wave propagation,
 237 known as the Stokes drift (Van Den Bremer and Breivik, 2018; Stokes,
 238 1880). This net drift has a significant impact on sediment transport in
 239 nearshore regions (Hoefel and Elgar, 2003), on the formation of Langmuir
 240 cells (Langmuir, 1938; Craik and Leibovich, 1976) as well as on the transport
 241 of heat, salt or pollutants such as oil or micro-plastic in the upper ocean layer
 242 (McWilliams and Sullivan, 2000; Röhrs et al., 2012; Drivdal et al., 2014). To
 243 correctly model the Stokes drift profile in mixed wind-driven sea and swell
 244 conditions, the full two-dimensional wave spectrum must be represented by a
 245 spectral wave model within a wave-current coupling (Van Den Bremer and
 246 Breivik, 2018). We therefore used SWAN modeled spectra to compute the
 247 Stokes drift as follows:

$$\mathbf{u}_s = \int_0^{2\pi} \int_0^{+\infty} \frac{\sigma^3}{h \tanh(2kh)} E(\sigma, \theta) (\cos \theta, \sin \theta) d\sigma d\theta , \quad (6)$$

248 where k is the norm of the wave vector; h is the water depth; and $E(\sigma, \theta)$ is
 249 the wave energy density. The computed Stokes drift velocity is then added to
 250 SLIM depth-averaged current velocity to transport drifting particles in the
 251 experiments described in section 2.6.

252 2.5. Coupled model

253 SLIM and SWAN are coupled so that they run on the same computational
 254 core and the same unstructured mesh. SLIM is run first and passes the
 255 wind velocity (\mathbf{U}_{10}), water level ($\eta = H - h$) and depth-averaged current
 256 ($\mathbf{u} = \mathbf{U}/H$) fields to SWAN, as well as a roughness length (z_0) for the bottom

257 dissipation formulation of Madsen et al. (1989). This roughness length is
258 computed from SLIM’s bulk drag coefficient C_b following the approach of
259 Dietrich et al. (2011) so that both models have consistent bottom dissipation
260 parameterizations. SWAN then uses these quantities to compute the wave
261 radiation stress gradient, that is then passed to SLIM as the force exerted
262 by waves on currents τ_{wave} (Fig. 3). SLIM then uses this quantity to update
263 the value of the surface stress τ_s in Eq. (1), that now becomes the sum of
264 wind and wave-induced stresses $\tau_s = \tau_{\text{wind}} + \tau_{\text{wave}}$. Here, the momentum
265 flux from the atmosphere to the ocean is taken as the usual full wind stress
266 τ_{wind} . Doing so, we neglect the momentum advected away from the storm
267 by the waves, leading to a 10-15% overestimation of the momentum flux in
268 hurricane winds (Curcic, 2015).

269 We followed the approach of Dietrich et al. (2012) by characterizing the
270 wave-induced forces on currents using the radiation-stress (RS) gradient
271 formalism, which has been successfully applied in both 2D and 3D coupled
272 wave-current models under storm conditions (Hope et al., 2013; Sebastian et al.,
273 2014; Brown et al., 2013). An alternative formalism is the vortex-force (VF)
274 representation (McWilliams et al., 2004), that provides a clearer decomposition
275 of the wave effect (Lane et al., 2007). Although both approaches were adopted
276 by coastal modeling communities, there is an ongoing scientific debate over the
277 correctness and applicability of the two concepts (Ardhuin et al., 2008; Mellor,
278 2013, 2015; Arduin et al., 2017). Xia et al. (2020) recently implemented the
279 two formalisms in a 3D unstructured-grid model and compared them in three
280 typical coastal systems, showing that the 3D RS algorithm could generate
281 unrealistic offshore currents near shorelines. Despite these shortcomings,
282 the 3D RS method reproduced most wave-induced currents and the 2D RS
283 formalism remains a well-validated modeling approach. Furthermore, Mellor
284 (2013) showed that the RS approach was valid when $[\frac{\partial H}{\partial x} / \sinh(kh)]^2$ is smaller
285 or of the same order as $(ka)^2$, where a is the wave amplitude. We evaluated
286 these quantities and verified that the validity criterion was met in our model

287 domain. Additionally, since the VF and RS approached are formally equivalent
288 (Lane et al., 2007), we selected the 2D RS formalism, as it has the advantage
289 of summarizing the impact of waves on the currents in a single additional
290 stress term in the hydrodynamic model equations.

291 SLIM's governing equations are integrated using an implicit time inte-
292 gration scheme while SWAN is unconditionally stable (Dietrich et al., 2012),
293 allowing both models to be run with relatively large time steps. In this study,
294 the stationary version of SWAN was used, *i.e.* the first term of Eq. (5) was
295 set to zero. This resulted in reduced scaling and convergence rates than
296 with the nonstationary version of SWAN but increased the model stability.
297 The wave spectra at each node of the mesh was saved at the end of each
298 iteration to serve as initial conditions for the next one. Both models were
299 run sequentially using a time step of 600 s, so that each computational core
300 was alternatively running either SLIM or SWAN. As in the coupling between
301 SWAN and the **ADvanced CIRCulation model** (ADCIRC) (Dietrich et al.,
302 2012), both models use the same local sub-mesh, allowing for a one-to-one
303 correspondence between the geographic locations of the mesh vertices. No
304 interpolation is therefore needed when passing the discretised variables from
305 one model to the other, which allows an efficient inter-model communication.
306 However, as SLIM is based on a discontinuous Galerkin finite element method,
307 an additional conversion step to a continuous framework was required to
308 transfer SLIM nodal quantities to SWAN. **The coupling increases the com-**
309 **putation time by 3% as compared to the sum of the uncoupled SLIM and**
310 **SWAN simulations wall-clock times for the same number of CPUs and the**
311 **same simulation period.**

312 *2.6. Quantifying the effect of wave-current interactions on transport*

313 To quantify the impact of wave-current interactions on transport processes,
314 we compared the trajectories of passive particles advected by the uncoupled
315 SLIM and coupled SLIM+SWAN currents during the passage of Irma in the
316 Lower Keys. Furthermore, the depth-averaged Stokes drift was computed

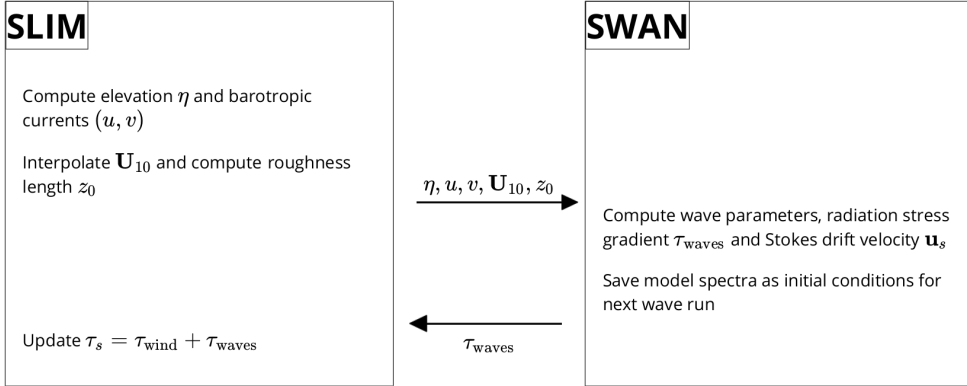


Fig. 3: Schematic illustration of the coupled SLIM+SWAN model.

317 using the wave spectra of the coupled model SLIM+SWAN run as well as
 318 those of an uncoupled SWAN run. Particles were released on the inner and
 319 outer shelves at the points highlighted by red and blue dots in Fig. 4 on
 320 Sept. 7 at 0000 UTC and then tracked until Sept. 15. These initial particle
 321 positions were found using backtracking methods (Spivakovskaya et al., 2005)
 322 to ensure that the release particles would intersect the path of Irma during
 323 its passage through the Florida Keys. We first defined two 25 km^2 circular
 324 regions on the trajectory of the hurricane (see red and blue circles in Fig. 4).
 325 Particles within these two regions were then tracked backward in time using
 326 uncoupled SLIM currents from the exact time of the passage of the hurricane
 327 until Sept. 7 at 0000 UTC. Their positions at the end of the backward
 328 simulation (see red and blue particle clouds in Fig. 4) corresponds to the
 329 initial condition of the forward transport simulations described below. We
 330 then compared the trajectories of particles originating from these regions and
 331 advected forward in time by different sets of currents: (i) uncoupled SLIM
 332 currents alone; (ii) coupled SLIM+SWAN currents; (iii) SLIM currents with
 333 the addition of the depth-averaged Stokes drift computed with the coupled
 334 wave-current model (Stokes-C); (iv) SLIM+SWAN currents with Stokes-C;
 335 and (v) SLIM currents with the depth-averaged Stokes drift computed with

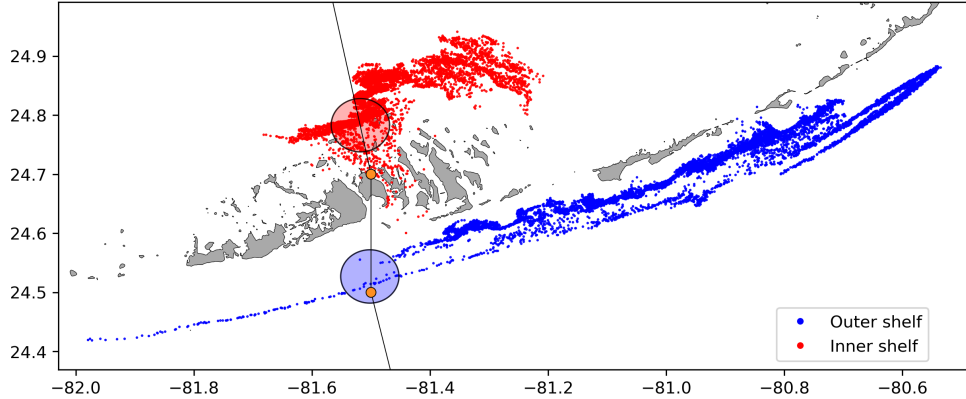


Fig. 4: Release regions of the passive particles on the inner and outer shelves on Sept 7 at 0000 UTC (red and blue clouds) obtained by backtracking particles released in the red and blue circular areas during the passage of Irma.

336 the uncoupled wave model (Stokes-U). The different combinations of Eulerian
 337 currents and Stokes drifts used to model the transport of passive drifters
 338 in the Lower Keys during the passage of Irma are summarized in Table 1.
 339 Particle trajectories are compared by computing the distances between the
 340 centers of mass of the particle clouds through time.

341 **3. Results**

342 We first validated the reconstructed atmospheric fields of Hurricane Irma
 343 as well as the outputs of our coupled wave-current model against field measure-
 344 ments. We then used the validated model outputs to simulate the transport
 345 of passive particles in the Lower Keys during the passage of Hurricane Irma.
 346 These particles were advected by the sets of currents described in Table 1 and
 347 their trajectories were compared to evaluate the impact of the wave-current
 348 interactions and the Stokes drift on the transport processes during the passage
 349 of Irma.

Experiment name	Eulerian currents from	Stokes drift from
SLIM	uncoupled SLIM simulation	None
SLIM+SWAN	coupled SLIM+SWAN simulation (impacted by RS gradient)	None
SLIM+Stokes-U	uncoupled SLIM simulation	uncoupled SWAN simulation
SLIM+Stokes-C	uncoupled SLIM simulation	coupled SLIM+SWAN simulation
SLIM+SWAN+Stokes-C	coupled SLIM+SWAN simulation (impacted by RS gradient)	coupled SLIM+SWAN simulation

Table 1: Summary of the different combinations of Eulerian currents and Stokes drifts used to model the transport of passive drifters on the passage of Hurricane Irma in the Lower Keys

350 *3.1. Model validation*

351 H*Wind winds and hybrid pressure field agree well with station mea-
 352 surements at Vaca Key station (Fig. 5). The hybrid pressure field shows a
 353 better agreement with observations than ERA-5 pressure as it successfully
 354 reproduces the storm depression. ERA-5 fields, on the other hand, fail to
 355 reproduce the low pressure at the core of the hurricane due to their coarser
 356 grid, leading to an overestimation of 8 mbar of the storm depression. Both
 357 H*Wind and ERA-5 agree well with observed wind speeds although both
 358 data sets tend to slightly overestimate the width and intensity of the wind
 359 peak. However, H*Wind profiles better reproduce the timing of the observed
 360 peak, as ERA-5 winds tend to anticipate it. H*wind also exhibits a slightly
 361 narrower peak in wind speed, which better agrees with observations.

362 Hydrodynamic outputs of the coupled wave-current model agree well with
 363 tide gauge (Fig. 6) and ADCP measurements (Fig. 7). The coupled model
 364 reproduces well the timing of the positive and negative storm surges at all

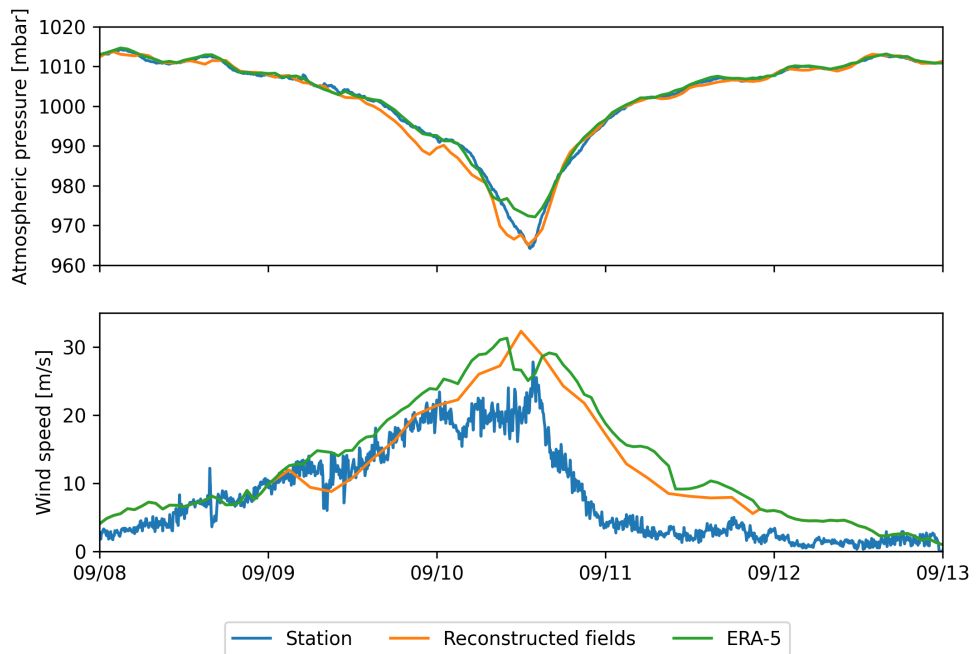


Fig. 5: Comparison of reconstructed atmospheric pressure (top) and wind speed (bottom) with field measurements and coarser ECMWF ERA-5 profiles at Vaca Key station. The generated hybrid atmospheric forcings better reproduce the observed storm depression while H*wind winds better reproduce the measured peak in wind speed.

365 tide gauge locations. The amplitude of the positive surges are especially
366 well captured at Naples and Vaca Key, with errors of 2 and 6 centimeters
367 respectively. However, the model underestimates the positive surges at
368 Virginia Key and Key West by 24% and 15% **at the peak** respectively. The
369 amplitude of the negative surge at Naples is also underestimated by about 16%
370 **at the peak**. Nonetheless, on average, the absolute error between the model
371 and observations does not exceed 10 cm (Table 2). Modeled 2D currents were
372 validated against depth-averaged ADCP measurements at mooring stations
373 C10, C12 and C13 (Fig. 7). As in Liu et al. (2020), we performed the
374 vector correlation analysis of Kundu (1976) to compare modeled and observed
375 current velocity vectors. Correlation coefficients (ρ) between simulated and
376 observed depth-averaged currents are 0.87, 0.84 and 0.81 at stations C10, C12
377 and C13, respectively. The average veering angles are below 12°, as in (Liu
378 et al., 2020). Furthermore, the positive bias in Table 2 indicates that our
379 model tends to underestimate the southward component of the currents at
380 the different stations. As expected from a depth-averaged model, the best fit
381 with observations is obtained at the shallowest mooring C10, located on the
382 25 m isobath.

383 The simulated significant wave height agrees well with observations at all
384 buoy locations (Fig. 8). The timing of the peak in wave height is well captured
385 at all buoys, while the amplitude is better reproduced on the WFS (buoys
386 42036 and 42097) with errors below 10%. The error on the peak amplitude on
387 Florida's eastern shelf is of 13% and 21% at buoys 4114 and 4113, respectively.
388 On average, observed significant wave height and wave period are better
389 reproduced on the WFS while wave direction is better captured by the model
390 on Florida's eastern shelf (Table 2). The fit is especially good at buoy 41113,
391 where the mostly westward-northwestward wave propagation is less perturbed
392 by Irma's wind field.

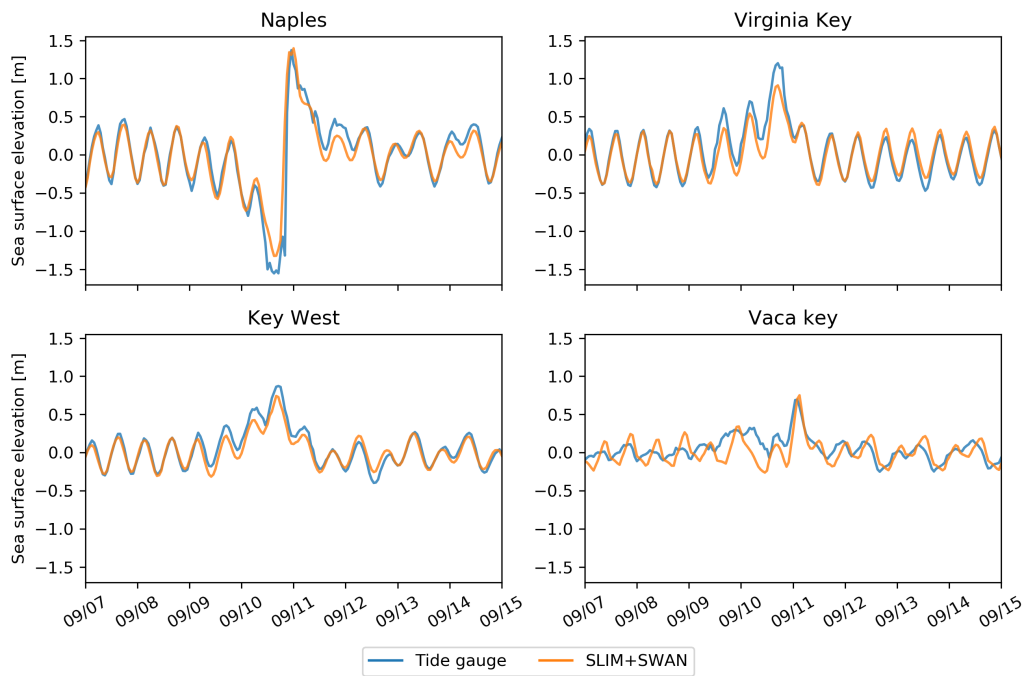


Fig. 6: Comparison of modeled sea surface elevation at the 4 tide gauges shown in Fig. 1B. The timing and amplitude of the storm surges are well reproduced by the model

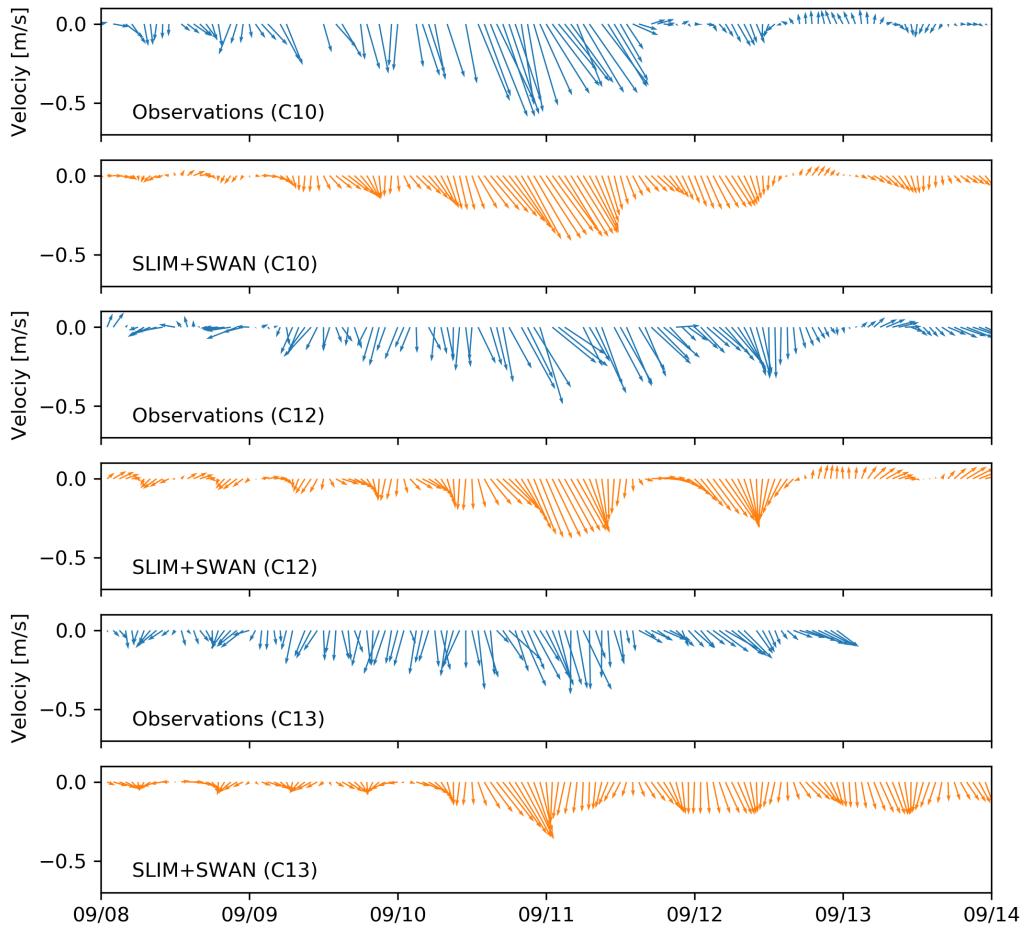


Fig. 7: Comparison of modeled current velocity with observed velocity at the moorings (see Fig. 1B for their location). Modeled current velocities agree well with observations, with a correlation coefficient of 0.87, 0.83 and 0.81 at moorings C10, C12 and C13, respectively. The corresponding veering angles are 5.4° , 0.07° and 10.5° , respectively.

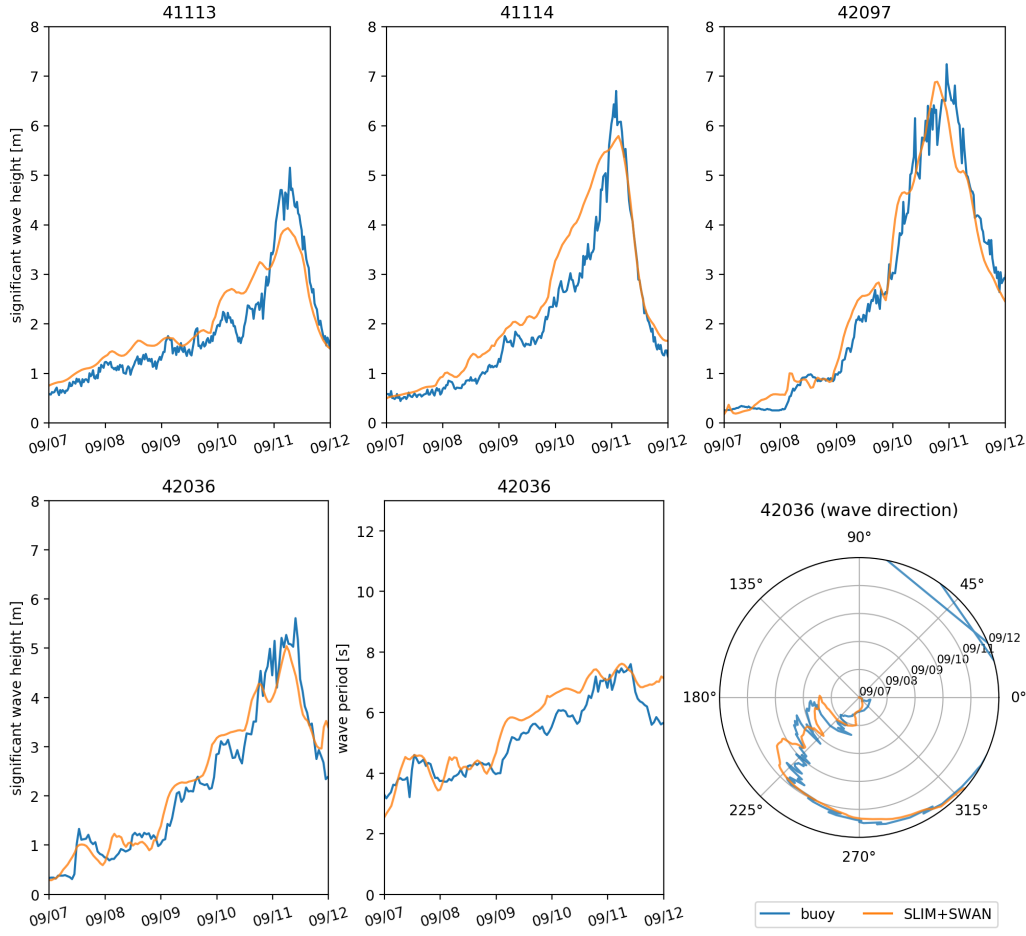


Fig. 8: Comparison of modeled wave parameters with observation at the 4 buoys location (locations shown in Fig. 1B). Overall, the modeled significant wave heights agree well with field measurement (mean error < 25%).

Station	Variable	Bias	MAE	RMSE
Vaca Key	sse (m)	0	0.112	0.142
	U_{10} (m/s)	1.51	1.85	2.61
	p_{atm} (hPa)	-0.21	0.59	1.03
Key West	sse (m)	0	0.066	0.085
Virginia Key	sse (m)	0	0.087	0.120
Naples	sse (m)	0	0.099	0.180
C10	u (m/s)	0.002	0.045	0.056
	v (m/s)	0.039	0.102	0.121
C12	u (m/s)	0.002	0.059	0.074
	v (m/s)	0.047	0.073	0.094
C13	u (m/s)	-0.009	0.065	0.077
	v (m/s)	0.039	0.086	0.102
41113	H_s (m)	0.150	0.357	0.430
	T_m (s)	1.608	1.671	1.878
	θ_m (degree)	-1.555	7.036	9.250
41114	H_s (m)	0.361	0.424	0.560
	T_m (s)	0.899	1.506	1.594
	θ_m (degree)	-8.236	14.616	22.560
42036	H_s (m)	0.082	0.312	0.398
	T_m (s)	0.430	0.528	0.645
	θ_m (degree)	-2.307	17.144	22.734
42097	H_s (m)	0.048	0.326	0.432
	T_m (s)	0.476	0.755	0.892
	θ_m (degree)	2.538	34.760	55.892

Table 2: Error statistics on the wave-current model outputs as compared to the measured sea surface elevation (sse), eastward and northward depth-average current velocities (u, v), significant wave height (H_s), zero-crossing mean wave period (T_m) and mean wave direction (θ_m). Model bias, mean absolute error (MAE), and root mean squared error (RMSE) are listed by variable (unit) and value.

393 *3.2. Impact of waves on currents and transport*

394 We evaluated the impact of the RS gradient on the modeled currents during
395 the passage of Irma in the Lower Keys, between Sept. 7 and 13, 2017. First,
396 we computed the maximum difference between currents modeled by SLIM and
397 SLIM+SWAN during this period (Fig. 9A). The largest differences in current
398 speed were observed over the reefs, on the shelf break and around islands. They
399 locally reach 1 m/s, with the coupled SLIM+SWAN model yielding the largest
400 amplitudes. The regions where the differences were the largest correspond
401 to areas that experienced large maximum values of the RS gradient τ_{wave}
402 (Fig. 9B). These areas of large RS gradient are located on the shelf break and
403 over coral reefs, where important wave energy dissipation occurred through
404 depth-induced wave breaking and bottom dissipation (Longuet-Higgins and
405 Stewart, 1964). This highlights the important protective role of the barrier
406 formed by the offshore reefs, that require a fine spatial resolution to be
407 accurately represented by the model. RS-induced differences in current speed
408 were amplified by the action of the wind stress τ_{wind} (Fig. 9C). Wind speeds
409 were larger in the front right quadrant of the hurricane (Zedler et al., 2009),
410 yielding larger differences on the right-hand side of the storm trajectory. This
411 is especially clear in the area between the Florida Keys and the Everglades,
412 where relatively small values of τ_{wave} produce current speed differences larger
413 than 0.5 m/s because of the wind stress.

414 Our results suggest that the RS gradient alone can deflect **particle** tra-
415 jectories by up to 1 km on the inner shelf and 5 km on the outer shelf (Fig.
416 10A,B). The RS mainly affects transport processes during the passage of
417 the hurricane, as the distance between particle cloud advected by SLIM and
418 SLIM+SWAN currents remains roughly constant afterwards. The Stokes
419 drift, however, has a longer-lasting effect on the particle trajectories on the
420 outer shelf. When adding a Stokes drift component to the Eulerian currents,
421 the distances between the particle cloud centers keeps increasing during 2
422 days after the passage of Irma (Fig. 10B). Under the effect of the Stokes drift,

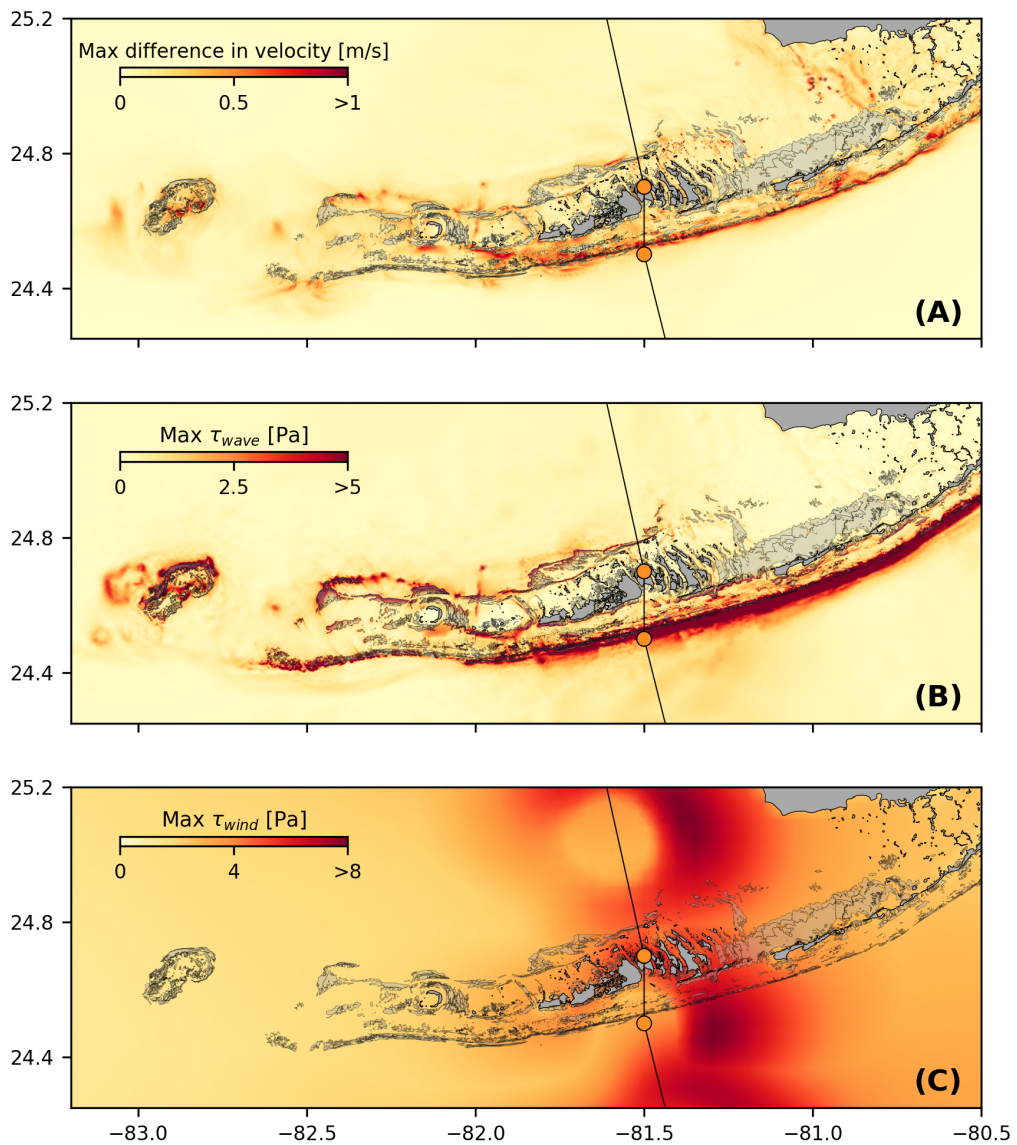


Fig. 9: (A). Maximum difference between SLIM and SLIM+SWAN currents during the passage of Irma in the Lower Florida Keys; (B) Maximum wave radiation stress gradient τ_{wave} and (C) maximum wind stress τ_{wind} (C) generated by the hurricane. Radiation stress gradient yields currents speed differences reaching 1 m/s, especially over offshore reefs.

423 particles from the outer shelf can be moved inshore on the passage of the
424 hurricane. This motion is less pronounced for particles that are advected by
425 Eulerian currents only. The particle cloud thus moves quickly northeastward
426 under the action of the FC. After 2 days, the particles advected inshore under
427 the action of the Stokes drift are in turn entrained by the FC and the distance
428 between the clouds of particles starts decreasing. The impact of the Stokes
429 drift on particle motion appears to be five times larger than the one of the
430 RS on the inner shelf (Fig. 10A). However, both processes yield a similar
431 impact on the particle trajectories at the moment of the passage of Hurricane
432 Irma on the outer shelf (Fig. 10B).

433 Taking wave-currents interactions into account appears to significantly
434 impact the modeled Stokes drift (Fig. 10C,D). Our results suggest that
435 neglecting the wave-current coupling when computing the Stokes drift in
436 storm conditions can yield deflections of the particle trajectories by up to 5
437 km on both the inner and outer shelves. On the outer shelf, differences in
438 particle trajectories mostly appear during the two days following the passage
439 of the hurricane. This is explained by the stronger shoreward component
440 of the coupled SLIM+SWAN Stokes drift compared to the uncoupled one.
441 On the inner shelf, however, differences in particle trajectories of up to 5 km
442 occur at the moment of the passage of Hurricane Irma. The distance between
443 the particle clouds then stabilizes directly after the passage of the hurricane.

444 4. Discussion

445 The coupled SLIM+SWAN model correctly reproduced the hydrodynamics
446 and wave dynamics during Hurricane Irma. Such good agreement with field
447 measurements could only be achieved using accurate forcings and adequate
448 wave parameterizations. By comparing coupled and uncoupled model runs, we
449 showed that neglecting wave radiation stress gradient can induce differences
450 of up to 1 m/s in modeled current velocities. The radiation stress gradient
451 during the hurricane was especially large over the shelf break, where waves

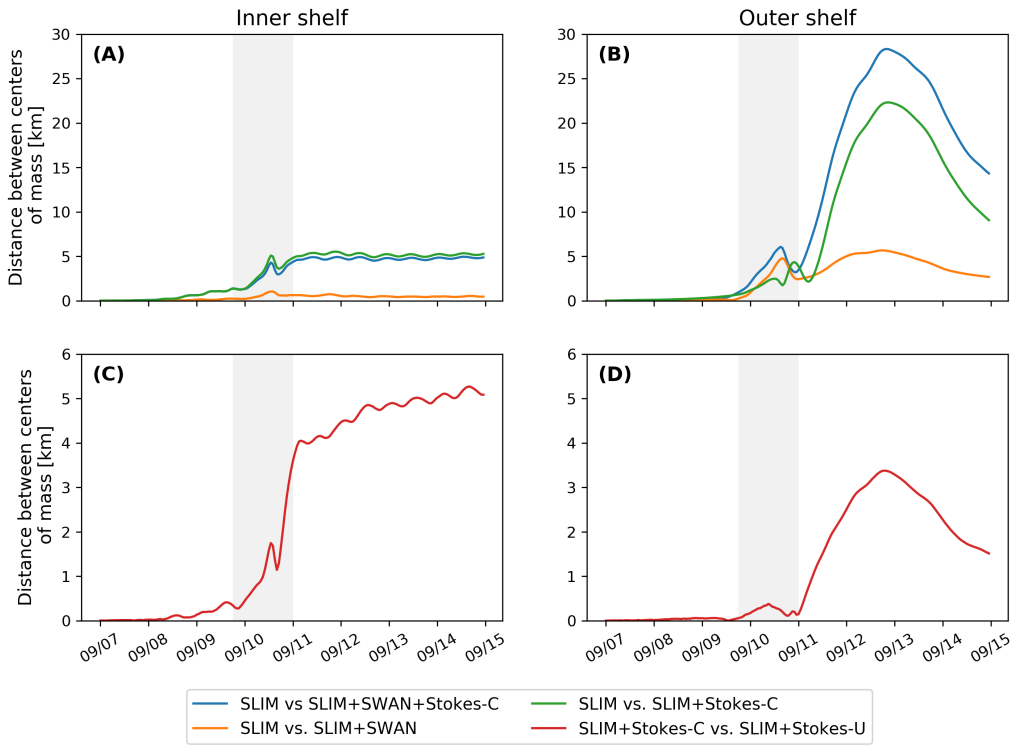


Fig. 10: Difference between the centers of mass of the particle clouds released from the regions highlighted in Fig. 4 and advected by the different combinations of Eulerian currents and Stokes drifts described in Table 1

452 are strongly dissipated by the offshore coral reef barrier. The radiation stress
453 gradient alone can deflect drifting particles by up to 5 km during the passage
454 of the hurricane. The impact of the Stokes drift dominates the effects of the
455 radiation stress gradient on transport processes, except during the passage of
456 the hurricane, when both contributions are similar on the outer shelf. The
457 Stokes drift induces a shoreward transport during the passage of the hurricane
458 that moves particles towards the inner shelf, **and** hence away from the FC.
459 Finally, neglecting wave-current interactions when computing Stokes drift
460 leads to variations of up to 5 km in modeled trajectories on the passage of
461 the hurricane.

462 The coupled wave-current model correctly reproduced the timing of the
463 observed storm surges and captured the elevation peaks with a 15% accuracy
464 at every tide gauge except Virginia Key. Such accuracy is key to predict the
465 damages caused by the hurricane, as they were mostly due to the storm surge
466 and high waves (Xian et al., 2018). Furthermore, by using a high-resolution
467 model, we can explicitly reproduce the circulation between all the reefs and
468 islands of the Florida Keys. The fine-scale details of the storm surge, and hence
469 the associated risk, are thus accurately represented. In addition to accurately
470 capturing positive surges, the model also reproduced the observed negative
471 surge in Naples. This result is of interest from a biological point of view as
472 negative surges, although less studied, affect water exchanges between the
473 estuaries and the coastal ocean and disturb the benthic ecosystems (Liu et al.,
474 2020). Such rapid decrease in water level followed by a positive surge cause
475 massive freshwater inflows, causing a significant decrease in water salinity
476 (Wachnicka et al., 2019). Surface waters are also significantly impacted by
477 storms and hurricanes through induced cooling, upwelling and mixing (Varlas
478 et al., 2020), but these processes were not accounted for in our model.

479 Strong currents such as the Gulf Stream affect waves **through** refraction
480 over gradients in current velocity, shoaling and breaking of opposing waves or
481 lengthening of following waves (Hegermiller et al., 2019). Under hurricane

482 conditions, these interactions can cause numerical instabilities in the wave
483 model if the parameterizations are not appropriate and the model resolution
484 not sufficient. Hegermiller et al. (2019), for instance, used a 5-km model
485 grid and 48 directional bins to capture spatial gradients in wave height
486 induced by wave-currents interactions in the Gulf Stream during Hurricane
487 Matthew (2016). We followed these guidelines when defining the coarsest mesh
488 resolution as the wave model spectral discretization. Boundary conditions and
489 directional spreading of the incident waves also play a significant role when
490 modeling wave-current interactions at meso- and submesoscales (Villas Bôas
491 et al., 2020), which motivated our choice of imposing full spectra on the
492 boundary of the wave model instead of bulk parameters.

493 Tropical cyclones interact with the Gulf Stream and the FC through
494 cooling and mixing of the upper ocean. These [interactions](#) can momentarily
495 disrupt these currents and cause a significant reduction of their transport (Oey
496 et al., 2007; Ezer et al., 2017; Ezer, 2020). As a 2D barotropic model, SLIM
497 does not explicitly capture the vertical structure of the FC and Gulf Stream.
498 Furthermore, a coupling with an atmospheric model would be required to
499 represent heat fluxes between the upper ocean and the hurricane. However,
500 we argue that a 2D model is sufficient for the scope of this study, that focuses
501 on nearshore processes on the shelf and the shelf slope. Furthermore, by
502 coupling the model with HYCOM, SLIM is able to represent indirectly the
503 baroclinic features such as the meandering of the FC and eddie formation
504 (Frys et al., 2020). Furthermore, using a 2D model allows us to capture the
505 impact of wave-current interactions on transport processes at the reef scale in
506 the topologically complex coastal system of the FRT. Such a fine resolution
507 is key to estimate the amount of wave energy dissipated over offshore reefs
508 and accurately capture the generated RS gradient.

509 The RS gradient significantly impacts currents during the passage of the
510 hurricane. It can induce differences of up to 1 m/s in the current speed on
511 the shelf break. In this region, waves are strongly dissipated due to action

of depth-induced breaking and bottom dissipation on coral reefs. This link between wave breaking, RS gradient and [wave-induced](#) nearshore currents is consistent with previous studies on wave-current dynamics during storms (Mao and Xia, 2017, 2018, 2020). Furthermore, our results highlight the protective role of coral reefs against strong incoming waves (Lowe et al., 2005), which requires a sufficiently fine spatial resolution to be explicitly represented in the model. As wave energy mostly dissipates on the shelf break, the impact of the RS gradient on transport processes is 5 times larger on the outer shelf. In the sheltered area of the inner shelf, wave impact on transport processes is dominated by the Stokes drift. Trajectory deflection under the influence of wave-induced motions mostly occurs at the moment of the passage of the hurricane on the inner shelf. After that moment, the distance between the clouds of particles remained roughly constant through time. On the outer shelf, RS and Stokes drift have a similar impact on transport processes at the moment of the passage of the cyclone and deflect particle trajectories by up to 5 km. However, by inducing shoreward transport, the Stokes drift delayed the advection of particles by the FC, therefore causing differences in trajectories of up to 20 km during the days following the passage of the hurricane. The dominance of the Stokes drift on particle transport in storm conditions was also observed in Lake Michigan by Mao and Xia (2020). Finally, neglecting wave-current coupling in Stokes drift computation leads to differences in modeled trajectories of the order of 5 km on both the inner and the outer shelves. This fact, coupled with the impact of RS-induced currents strongly advocates for the use of coupled wave-current models when studying transport processes in storm conditions.

537 5. Conclusion

We developed a coupled wave-current model to study the impact of waves on transport processes during Hurricane Irma. In order to accurately represent the wind and pressure profiles of the hurricane, we built hybrid fields by

541 combining coarser ERA-5 data with high-resolution H*Wind data for the wind
542 speed and idealized Holland profiles for the pressure. Comparing these hybrid
543 profiles with field observations showed that they were better at reproducing the
544 observed central depression of the hurricane as well as the peak in wind speed
545 than ERA-5 data. Using these hybrid fields as forcings, our coupled model
546 accurately reproduced the storm surge at tide gauge locations and produced
547 currents and wave parameters in good agreement with field observations. The
548 modeled currents and Stokes drift were then used to evaluate the impact of
549 wave-current coupling on the modeled trajectories of passive drifters on the
550 passage of the hurricane through the Florida Keys. Our results show that
551 waves had a significant impact on heavy-wind transport processes and caused
552 deflections of the drifters trajectories by more than 20 km on the outer shelf.

553 Despite its good agreement with observations, our model could be further
554 refined by improving the representation of wind-wave interactions. In particu-
555 lar, we did not consider the momentum loss due to the action of surface waves,
556 which can lead to overestimations of the momentum flux from the atmosphere
557 to the ocean under hurricane conditions. Our model could therefore be further
558 improved by using a wave-dissipative stress instead of the full wind stress as
559 the momentum flux from the atmosphere to the ocean. As a 2D barotropic
560 model, SLIM does not explicitly represent heat fluxes between the ocean and
561 the atmosphere and the vertical structure of the ocean. However, our study
562 focused on relatively shallow and vertically homogeneous coastal waters using
563 a reef-scale resolution throughout the whole FRT. Such fine resolution allows
564 to explicitly represent wave dissipation over coral reefs and is only achievable
565 using a 2D model due to computational resource limitations.

566 Wave coupling needs to be taken into account during heavy-wind events
567 but not necessarily in milder conditions. While the RS gradient plays an
568 important role and can lead to differences of up to 5 km, the Stokes drift is
569 about 4 times more intense and is thus the most important wave-induced
570 transport process. Nonetheless, neglecting wave-current coupling through RS

571 when modeling Stokes drift leads to differences of up to 5 km in predicted
572 drifter trajectories. Such discrepancies reveal the strong influence of wave-
573 current interactions on transport under storm conditions. This study brings
574 new insight on the impact of waves on the transport processes nearshore
575 during a tropical cyclone. Due to its fine spatial resolution, our coupled wave-
576 current model can be used to accurately represent the dispersal of pollutants,
577 sediments or larvae in topologically complex coastal areas in heavy-wind
578 conditions.

579 Acknowledgments

580 Computational resources were provided by the Consortium des Équipements
581 de Calcul Intensif (CÉCI), funded by the F.R.S.-FNRS under Grant No.
582 2.5020.11. Thomas Dobbelaere is a PhD student supported by the Fund for
583 Research training in Industry and Agriculture (FRIA/FNRS).

584 This work was also supported by the Disaster Related Appropriation
585 Supplemental: Improving Forecasting and Assimilation (DRAS 19 IFAA),
586 awarded to the University of Miami under award NA19OAR0220184. It was
587 also supported by the FY19 Disaster Supplemental: Improving Forecasting of
588 Hurricanes, Floods, and Wildfires (FY19 IFHFW) awarded to the University
589 of Miami under award NA20OAR4600263. M. Le Hénaff received partial
590 support for work on this publication by NOAA/AOML, and was partly
591 supported under the auspices of the Cooperative Institute for Marine and
592 Atmospheric Studies (CIMAS), a cooperative institute of the University of
593 Miami and NOAA, cooperative agreement NA20OAR4320472.

594 References

595 Abdolali, A., Roland, A., Van Der Westhuysen, A., Meixner, J., Chawla,
596 A., Hesser, T.J., Smith, J.M., Sikiric, M.D., 2020. Large-scale hurricane
597 modeling using domain decomposition parallelization and implicit scheme

- 598 implemented in WAVEWATCH III wave model. Coastal Engineering 157,
599 103656.
- 600 Aijaz, S., Ghantous, M., Babanin, A., Ginis, I., Thomas, B., Wake, G., 2017.
601 Nonbreaking wave-induced mixing in upper ocean during tropical cyclones
602 using coupled hurricane-ocean-wave modeling. Journal of Geophysical
603 Research: Oceans 122, 3939–3963.
- 604 Arduin, F., Jenkins, A.D., Belibassakis, K.A., 2008. Comments on “The
605 three-dimensional current and surface wave equations”. Journal of Physical
606 Oceanography 38, 1340–1350.
- 607 Arduin, F., Suzuki, N., McWilliams, J.C., Aiki, H., 2017. Comments on
608 “A combined derivation of the integrated and vertically resolved, coupled
609 wave–current equations”. Journal of Physical Oceanography 47, 2377–2385.
- 610 Bever, A.J., MacWilliams, M.L., 2013. Simulating sediment transport pro-
611 cesses in San Pablo Bay using coupled hydrodynamic, wave, and sediment
612 transport models. Marine Geology 345, 235–253.
- 613 Bhatia, K.T., Vecchi, G.A., Knutson, T.R., Murakami, H., Kossin, J., Dixon,
614 K.W., Whitlock, C.E., 2019. Recent increases in tropical cyclone intensifi-
615 cation rates. Nature Communications 10, 1–9.
- 616 Booij, N., Ris, R.C., Holthuijsen, L.H., 1999. A third-generation wave
617 model for coastal regions: 1. Model description and validation. Journal of
618 Geophysical Research: Oceans 104, 7649–7666.
- 619 Breivik, Ø., Allen, A.A., Maisondieu, C., Olagnon, M., 2013. Advances in
620 search and rescue at sea. Ocean Dynamics 63, 83–88.
- 621 Brown, J.M., Bolaños, R., Wolf, J., 2013. The depth-varying response of
622 coastal circulation and water levels to 2D radiation stress when applied
623 in a coupled wave–tide–surge modelling system during an extreme storm.
624 Coastal Engineering 82, 102–113.

- 625 Cangialosi, J.P., Latto, A.S., Berg, R., 2018. National Hurricane Center
626 Tropical Cyclone Report: Hurricane Irma (30 August–12 September 2017).
627 https://www.nhc.noaa.gov/data/tcr/AL112017_Irma.pdf.
- 628 Chassignet, E.P., Hurlburt, H.E., Smedstad, O.M., Halliwell, G.R., Hogan,
629 P.J., Wallcraft, A.J., Baraille, R., Bleck, R., 2007. The HYCOM (hybrid
630 coordinate ocean model) data assimilative system. *Journal of Marine
631 Systems* 65, 60–83.
- 632 Craik, A.D., Leibovich, S., 1976. A rational model for Langmuir circulations.
633 *Journal of Fluid Mechanics* 73, 401–426.
- 634 Curcic, M., 2015. Explicit air-sea momentum exchange in coupled atmosphere-
635 wave-ocean modeling of tropical cyclones. Ph.D. thesis. University of Miami.
- 636 Curcic, M., Chen, S.S., Özgökmen, T.M., 2016. Hurricane-induced ocean
637 waves and stokes drift and their impacts on surface transport and dispersion
638 in the Gulf of Mexico. *Geophysical Research Letters* 43, 2773–2781.
- 639 Curcic, M., Haus, B.K., 2020. Revised estimates of ocean surface drag in
640 strong winds. *Geophysical Research Letters* 47, e2020GL087647.
- 641 Dietrich, J., Bunya, S., Westerink, J., Ebersole, B., Smith, J., Atkinson,
642 J., Jensen, R., Resio, D., Luettich, R., Dawson, C., et al., 2010. A high-
643 resolution coupled riverine flow, tide, wind, wind wave, and storm surge
644 model for southern Louisiana and Mississippi. Part II: Synoptic description
645 and analysis of Hurricanes Katrina and Rita. *Monthly Weather Review*
646 138, 378–404.
- 647 Dietrich, J., Westerink, J., Kennedy, A., Smith, J., Jensen, R., Zijlema, M.,
648 Holthuijsen, L., Dawson, C., Luettich, R., Powell, M., et al., 2011. Hurricane
649 Gustav (2008) waves and storm surge: Hindcast, synoptic analysis, and
650 validation in southern Louisiana. *Monthly Weather Review* 139, 2488–2522.

- 651 Dietrich, J.C., Tanaka, S., Westerink, J.J., Dawson, C., Luettich, R., Zijlema,
652 M., Holthuijsen, L.H., Smith, J., Westerink, L., Westerink, H., 2012. Performance of the unstructured-mesh, SWAN+ ADCIRC model in computing
653 hurricane waves and surge. *Journal of Scientific Computing* 52, 468–497.
- 655 Dobbelaere, T., Muller, E.M., Gramer, L.J., Holstein, D.M., Hanert, E., 2020.
656 Coupled epidemi-hydrodynamic modeling to understand the spread of a
657 deadly coral disease in Florida. *Frontiers in Marine Science* 7, 1016.
- 658 Donelan, M., Haus, B., Reul, N., Plant, W., Stiassnie, M., Graber, H., Brown,
659 O., Saltzman, E., 2004. On the limiting aerodynamic roughness of the
660 ocean in very strong winds. *Geophysical Research Letters* 31.
- 661 Drivdal, M., Broström, G., Christensen, K., 2014. Wave-induced mixing and
662 transport of buoyant particles: Application to the Statfjord A oil spill.
663 *Ocean Science* 10, 977–991.
- 664 Ezer, T., 2018. On the interaction between a hurricane, the Gulf Stream and
665 coastal sea level. *Ocean Dynamics* 68, 1259–1272.
- 666 Ezer, T., 2020. The long-term and far-reaching impact of hurricane dorian
667 (2019) on the gulf stream and the coast. *Journal of Marine Systems* 208,
668 103370.
- 669 Ezer, T., Atkinson, L.P., Tuleya, R., 2017. Observations and operational
670 model simulations reveal the impact of Hurricane Matthew (2016) on the
671 Gulf Stream and coastal sea level. *Dynamics of Atmospheres and Oceans*
672 80, 124–138.
- 673 Figueiredo, J., Baird, A.H., Connolly, S.R., 2013. Synthesizing larval com-
674 petence dynamics and reef-scale retention reveals a high potential for
675 self-recruitment in corals. *Ecology* 94, 650–659.

- 676 Fringer, O.B., Dawson, C.N., He, R., Ralston, D.K., Zhang, Y.J., 2019. The
677 future of coastal and estuarine modeling: Findings from a workshop. *Ocean*
678 *Modelling* 143, 101458.
- 679 Frys, C., Saint-Amand, A., Le Hénaff, M., Figueiredo, J., Kuba, A., Walker,
680 B., Lambrechts, J., Vallaey, V., Vincent, D., Hanert, E., 2020. Fine-scale
681 coral connectivity pathways in the Florida Reef Tract: Implications for
682 conservation and restoration. *Frontiers in Marine Science* 7, 312.
- 683 Geuzaine, C., Remacle, J.F., 2009. Gmsh: A 3-d finite element mesh generator
684 with built-in pre-and post-processing facilities. *International journal for*
685 *numerical methods in engineering* 79, 1309–1331.
- 686 Harper, B., Kepert, J., Ginger, J., 2010. Guidelines for converting between
687 various wind averaging periods in tropical cyclone conditions.
- 688 Hegermiller, C.A., Warner, J.C., Olabarrieta, M., Sherwood, C.R., 2019.
689 Wave-current interaction between Hurricane Matthew wave fields and the
690 Gulf Stream. *Journal of Physical Oceanography* 49, 2883–2900.
- 691 Hoefel, F., Elgar, S., 2003. Wave-induced sediment transport and sandbar
692 migration. *Science* 299, 1885–1887.
- 693 Holthuijsen, L.H., Powell, M.D., Pietrzak, J.D., 2012. Wind and waves in
694 extreme hurricanes. *Journal of Geophysical Research: Oceans* 117.
- 695 Hope, M.E., Westerink, J.J., Kennedy, A.B., Kerr, P., Dietrich, J.C., Dawson,
696 C., Bender, C.J., Smith, J., Jensen, R.E., Zijlema, M., et al., 2013. Hindcast
697 and validation of Hurricane ike (2008) waves, forerunner, and storm surge.
698 *Journal of Geophysical Research: Oceans* 118, 4424–4460.
- 699 Janssen, P.A., 1991. Quasi-linear theory of wind-wave generation applied to
700 wave forecasting. *Journal of Physical Oceanography* 21, 1631–1642.

- 701 Johns, W.E., Schott, F., 1987. Meandering and transport variations of the
702 Florida Current. *Journal of Physical Oceanography* 17, 1128–1147.
- 703 Knaff, J.A., Sampson, C.R., Musgrave, K.D., 2018. Statistical tropical cyclone
704 wind radii prediction using climatology and persistence: Updates for the
705 western North Pacific. *Weather and Forecasting* 33, 1093–1098.
- 706 Knutson, T., Camargo, S.J., Chan, J.C., Emanuel, K., Ho, C.H., Kossin, J.,
707 Mohapatra, M., Satoh, M., Sugi, M., Walsh, K., et al., 2020. Tropical
708 cyclones and climate change assessment: Part II: Projected response to
709 anthropogenic warming. *Bulletin of the American Meteorological Society*
710 101, E303–E322.
- 711 Komen, G., Hasselmann, S., Hasselmann, K., 1984. On the existence of a
712 fully developed wind-sea spectrum. *Journal of Physical Oceanography* 14,
713 1271–1285.
- 714 Kourafalou, V.H., Kang, H., 2012. Florida Current meandering and evo-
715 lution of cyclonic eddies along the Florida Keys Reef Tract: Are they
716 interconnected? *Journal of Geophysical Research: Oceans* 117.
- 717 Kundu, P.K., 1976. Ekman veering observed near the ocean bottom. *Journal*
718 *of Physical Oceanography* 6, 238–242.
- 719 Lambrechts, J., Hanert, E., Deleersnijder, E., Bernard, P.E., Legat, V.,
720 Remacle, J.F., Wolanski, E., 2008. A multi-scale model of the hydrodynam-
721 ics of the whole Great Barrier Reef. *Estuarine, Coastal and Shelf Science*
722 79, 143–151.
- 723 Landsea, C.W., Franklin, J.L., 2013. Atlantic hurricane database uncertainty
724 and presentation of a new database format. *Monthly Weather Review* 141,
725 3576–3592.

- 726 Lane, E.M., Restrepo, J., McWilliams, J.C., 2007. Wave-current interaction:
727 A comparison of radiation-stress and vortex-force representations. *Journal*
728 *of Physical Oceanography* 37, 1122–1141.
- 729 Langmuir, I., 1938. Surface motion of water induced by wind. *Science* 87,
730 119–123.
- 731 Le, H.A., Lambrechts, J., Ortaleb, S., Gratiot, N., Deleersnijder, E., Soares-
732 Frazão, S., 2020. An implicit wetting–drying algorithm for the discontinuous
733 galerkin method: application to the tonle sap, mekong river basin. *Envi-*
734 *ronmental Fluid Mechanics* , 1–29.
- 735 Le Hénaff, M., Kourafalou, V.H., Paris, C.B., Helgers, J., Aman, Z.M., Hogan,
736 P.J., Srinivasan, A., 2012. Surface evolution of the Deepwater Horizon
737 oil spill patch: Combined effects of circulation and wind-induced drift.
738 *Environmental Science & Technology* 46, 7267–7273.
- 739 Lee, T.N., Leaman, K., Williams, E., Berger, T., Atkinson, L., 1995. Florida
740 Current meanders and gyre formation in the southern Straits of Florida.
741 *Journal of Geophysical Research: Oceans* 100, 8607–8620.
- 742 Lee, T.N., Mayer, D.A., 1977. Low-frequency current variability and spin-off
743 eddies along the shelf off southeast Florida. *Collected Reprints* 1, 344.
- 744 Lee, T.N., Smith, N., 2002. Volume transport variability through the Florida
745 Keys tidal channels. *Continental Shelf Research* 22, 1361–1377.
- 746 Lee, T.N., Williams, E., 1988. Wind-forced transport fluctuations of the
747 Florida Current. *Journal of Physical Oceanography* 18, 937–946.
- 748 Li, Z., Johns, B., 1998. A three-dimensional numerical model of surface
749 waves in the surf zone and longshore current generation over a plane beach.
750 *Estuarine, Coastal and Shelf Science* 47, 395–413.

- 751 Lin, N., Chavas, D., 2012. On hurricane parametric wind and applications in
752 storm surge modeling. *Journal of Geophysical Research: Atmospheres* 117.
- 753 Liu, Y., Weisberg, R.H., 2012. Seasonal variability on the West Florida shelf.
754 *Progress in Oceanography* 104, 80–98.
- 755 Liu, Y., Weisberg, R.H., Zheng, L., 2020. Impacts of hurricane Irma on the
756 circulation and transport in Florida Bay and the Charlotte Harbor estuary.
757 *Estuaries and Coasts* 43, 1194–1216.
- 758 Liubartseva, S., Coppini, G., Lecci, R., Clementi, E., 2018. Tracking plastics
759 in the Mediterranean: 2D Lagrangian model. *Marine Pollution Bulletin*
760 129, 151–162.
- 761 Longuet-Higgins, M.S., 1970. Longshore currents generated by obliquely
762 incident sea waves. *Journal of Geophysical Research* 75, 6778–6789.
- 763 Longuet-Higgins, M.S., Stewart, R., 1964. Radiation stresses in water waves;
764 a physical discussion, with applications, in: *Deep Sea Research and Oceanographic Abstracts*, Elsevier. pp. 529–562.
- 766 Lowe, R.J., Falter, J.L., Bandet, M.D., Pawlak, G., Atkinson, M.J., Moni-
767 smith, S.G., Koseff, J.R., 2005. Spectral wave dissipation over a barrier
768 reef. *Journal of Geophysical Research: Oceans* 110.
- 769 Madsen, O.S., Poon, Y.K., Gruber, H.C., 1989. Spectral wave attenuation by
770 bottom friction: Theory, in: *Coastal Engineering 1988*, pp. 492–504.
- 771 Malmstadt, J., Scheitlin, K., Elsner, J., 2009. Florida hurricanes and damage
772 costs. *Southeastern Geographer* 49, 108–131.
- 773 Mao, M., Xia, M., 2017. Dynamics of wave–current–surge interactions in lake
774 michigan: A model comparison. *Ocean Modelling* 110, 1–20.

- 775 Mao, M., Xia, M., 2018. Wave–current dynamics and interactions near the
776 two inlets of a shallow lagoon–inlet–coastal ocean system under hurricane
777 conditions. *Ocean Modelling* 129, 124–144.
- 778 Mao, M., Xia, M., 2020. Particle dynamics in the nearshore of Lake Michi-
779 gan revealed by an observation-modeling system. *Journal of Geophysical*
780 *Research: Oceans* 125, e2019JC015765.
- 781 McWilliams, J.C., Restrepo, J.M., Lane, E.M., 2004. An asymptotic theory
782 for the interaction of waves and currents in coastal waters. *Journal of Fluid*
783 *Mechanics* 511, 135.
- 784 McWilliams, J.C., Sullivan, P.P., 2000. Vertical mixing by Langmuir circula-
785 tions. *Spill Science & Technology Bulletin* 6, 225–237.
- 786 Mei, C.C., 1989. The applied dynamics of ocean surface waves. volume 1.
787 World scientific.
- 788 Mellor, G., 2013. Waves, circulation and vertical dependence. *Ocean Dynamics*
789 63, 447–457.
- 790 Mellor, G., 2015. A combined derivation of the integrated and vertically re-
791 solved, coupled wave–current equations. *Journal of Physical Oceanography*
792 45, 1453–1463.
- 793 Moon, I.J., Ginis, I., Hara, T., Thomas, B., 2007. A physics-based parame-
794 terization of air–sea momentum flux at high wind speeds and its impact on
795 hurricane intensity predictions. *Monthly Weather Review* 135, 2869–2878.
- 796 Niu, Q., Xia, M., 2017. The role of wave-current interaction in Lake Erie’s
797 seasonal and episodic dynamics. *Journal of Geophysical Research: Oceans*
798 122, 7291–7311.

- 799 Oey, L.Y., Ezer, T., Wang, D.P., Yin, X.Q., Fan, S.J., 2007. Hurricane-
800 induced motions and interaction with ocean currents. *Continental Shelf*
801 *Research* 27, 1249–1263.
- 802 Pinelli, J.P., Roueche, D., Kijewski-Correa, T., Plaz, F., Prevatt, D., Zisis,
803 I., Elawady, A., Haan, F., Pei, S., Gurley, K., et al., 2018. Overview of
804 damage observed in regional construction during the passage of Hurricane
805 Irma over the State of Florida, in: *Forensic Engineering 2018: Forging*
806 *Forensic Frontiers*. American Society of Civil Engineers Reston, VA, pp.
807 1028–1038.
- 808 Powell, M.D., Houston, S.H., Amat, L.R., Morisseau-Leroy, N., 1998. The
809 HRD real-time hurricane wind analysis system. *Journal of Wind Engineering*
810 and *Industrial Aerodynamics* 77, 53–64.
- 811 Powell, M.D., Vickery, P.J., Reinhold, T.A., 2003. Reduced drag coefficient
812 for high wind speeds in tropical cyclones. *Nature* 422, 279–283.
- 813 Röhrs, J., Christensen, K.H., Hole, L.R., Broström, G., Drivdal, M., Sundby,
814 S., 2012. Observation-based evaluation of surface wave effects on currents
815 and trajectory forecasts. *Ocean Dynamics* 62, 1519–1533.
- 816 Schott, F.A., Lee, T.N., Zantopp, R., 1988. Variability of structure and
817 transport of the Florida Current in the period range of days to seasonal.
818 *Journal of Physical Oceanography* 18, 1209–1230.
- 819 Sebastian, A., Proft, J., Dietrich, J.C., Du, W., Bedient, P.B., Dawson, C.N.,
820 2014. Characterizing hurricane storm surge behavior in Galveston Bay
821 using the swan+ adcirc model. *Coastal Engineering* 88, 171–181.
- 822 Siadatmousavi, S.M., Jose, F., Stone, G., 2011. Evaluation of two WAM
823 white capping parameterizations using parallel unstructured SWAN with
824 application to the Northern Gulf of Mexico, USA. *Applied Ocean Research*
825 33, 23–30.

- 826 Sikirić, M.D., Roland, A., Janeković, I., Tomazić, I., Kuzmić, M., 2013.
827 Coupling of the Regional Ocean Modeling System (ROMS) and Wind
828 Wave Model. *Ocean Modelling* 72, 59–73.
- 829 Smith, N.P., 1982. Response of Florida Atlantic shelf waters to hurricane
830 David. *Journal of Geophysical Research: Oceans* 87, 2007–2016.
- 831 Spivakovskaya, D., Heemink, A., Milstein, G., Schoenmakers, J., 2005. Sim-
832 ulation of the transport of particles in coastal waters using forward and
833 reverse time diffusion. *Advances in water resources* 28, 927–938.
- 834 Stokes, G.G., 1880. On the theory of oscillatory waves. *Transactions of the*
835 *Cambridge Philosophical Society* .
- 836 Tolman, H.L., et al., 2009. User manual and system documentation of
837 WAVEWATCH III TM version 3.14. Technical note, MMAB Contribution
838 276, 220.
- 839 Van Den Bremer, T., Breivik, Ø., 2018. Stokes drift. *Philosophical Trans-*
840 *actions of the Royal Society A: Mathematical, Physical and Engineering*
841 *Sciences* 376, 20170104.
- 842 Varlas, G., Vervatis, V., Spyrou, C., Papadopoulou, E., Papadopoulos, A.,
843 Katsafados, P., 2020. Investigating the impact of atmosphere–wave–ocean
844 interactions on a Mediterranean tropical-like cyclone. *Ocean Modelling* 153,
845 101675.
- 846 Villas Bôas, A.B., Cornuelle, B.D., Mazloff, M.R., Gille, S.T., Arduin, F.,
847 2020. Wave–current interactions at meso-and submesoscales: Insights from
848 idealized numerical simulations. *Journal of Physical Oceanography* 50,
849 3483–3500.
- 850 Wachnicka, A., Browder, J., Jackson, T., Louda, W., Kelble, C., Abdelrahman,
851 O., Stabenau, E., Avila, C., 2019. Hurricane Irma’s impact on water quality

- 852 and phytoplankton communities in Biscayne Bay (Florida, USA). *Estuaries*
853 and Coasts , 1–18.
- 854 WAMDI Group, 1988. The WAM model – A third generation ocean wave
855 prediction model. *Journal of Physical Oceanography* 18, 1775–1810.
- 856 Warner, J.C., Armstrong, B., He, R., Zambon, J.B., 2010. Development of a
857 coupled ocean–atmosphere–wave–sediment transport (COAWST) modeling
858 system. *Ocean modelling* 35, 230–244.
- 859 Weisberg, R., Liu, Y., Mayer, D., 2009. Mean circulation on the west Florida
860 continental shelf observed with long-term moorings. *Geophys. Res. Lett*
861 36, L19610.
- 862 Weisberg, R.H., Zheng, L., 2006. Hurricane storm surge simulations for
863 Tampa Bay. *Estuaries and Coasts* 29, 899–913.
- 864 Wu, L., Chen, C., Guo, P., Shi, M., Qi, J., Ge, J., 2011. A FVCOM-
865 based unstructured grid wave, current, sediment transport model, I. Model
866 description and validation. *Journal of Ocean University of China* 10, 1–8.
- 867 WW3DG, 2019. User Manual and System Documentation of WAVEWATCH
868 III Version 6.07, the WAVEWATCH III Development Group. Technical Note
869 316. NOAA/NWS/ NCEP/MMAB url: <https://github.com/NOAA-EMC/WW3/wiki/files/manual.pdf>.
- 871 Xia, M., Mao, M., Niu, Q., 2020. Implementation and comparison of the
872 recent three-dimensional radiation stress theory and vortex-force formalism
873 in an unstructured-grid coastal circulation model. *Estuarine, Coastal and*
874 *Shelf Science* 240, 106771.
- 875 Xian, S., Feng, K., Lin, N., Marsooli, R., Chavas, D., Chen, J., Hatzikyriakou,
876 A., 2018. Brief communication: Rapid assessment of damaged residential
877 buildings in the Florida Keys after Hurricane Irma. *Natural Hazards and*
878 *Earth System Sciences* 18, 2041–2045.

- 879 Zedler, S., Niiler, P., Stammer, D., Terrill, E., Morzel, J., 2009. Ocean's
880 response to Hurricane Frances and its implications for drag coefficient
881 parameterization at high wind speeds. *Journal of Geophysical Research: Oceans* 114.
- 883 Zhang, C., Durgan, S.D., Lagomasino, D., 2019. Modeling risk of mangroves
884 to tropical cyclones: A case study of Hurricane Irma. *Estuarine, Coastal
885 and Shelf Science* 224, 108–116.